

3D MC II: X-ray echoes reveal a clumpy molecular cloud in the CMZ

DANYA ALBOSLANI,¹ CARA BATTERSBY,¹ SAMANTHA W. BRUNKER,¹ MAÏCA CLAVEL,² DANI LIPMAN,¹ AND DANIEL L. WALKER^{1,3}

¹University of Connecticut, Department of Physics, 196A Auditorium Road, Unit 3046, Storrs, CT 06269, USA

²Univ. Grenoble Alpes, CNRS, IPAG, F-38000 Grenoble, France

³ALMA Regional Centre Node, Jodrell Bank Centre for Astrophysics, The University of Manchester, Manchester M13 9PL, UK

ABSTRACT

X-ray observations collected over the last decades have revealed a strongly variable X-ray signal within the Milky Way’s Galactic center, interpreted as X-ray echoes from its supermassive black hole, Sgr A*. These echoes are traced by the strong Fe K α fluorescent line at 6.4 keV of which its intensity is proportional to the density of the illuminated molecular gas. Over time, the echo scans through molecular clouds (MCs) in our Galactic center, revealing their 3D structure and highlighting their densest parts. While previous studies have utilized spectral line doppler shifts along with kinematic models to constrain the geometry of the CMZ or to study the structure of individual clouds, these methods have limitations, particularly in the turbulent region of the CMZ. We use archival Chandra X-ray data to construct one of the first 3D representations of one prominent MC, the Stone Cloud, located at ($l = 0.068^\circ$, $b = -0.076^\circ$) at a distance of ~ 20 pc from Sgr A* in projection. Using the *Chandra X-ray Observatory*, we followed the X-ray echo in this cloud from 2008 to 2017. We combine this data with 1.3 mm dust continuum emission observed with the Submillimeter Array (SMA) and the *Herschel Space Observatory* to re-construct the 3D structure of the cloud and estimate the column densities for each year’s observed slice. The analysis of the X-ray echoes along with velocities from SMA molecular line data indicate that the structure of the Stone cloud can be described as a very diffuse background with multiple dense clumps throughout.

1. INTRODUCTION

The inner ~ 300 pc of the Milky Way’s Galactic center, the Central Molecular Zone (CMZ), is often characterized as an extreme environment with molecular hydrogen contained in molecular clouds (MCs) with gas densities exceeding 10^4 cm $^{-3}$ (e.g. Guesten & Henkel 1983; Mills et al. 2018), gas temperatures of 50-100 K (Ginsburg et al. 2016; Krieger et al. 2017), intense magnetic fields of 10-1000 μ G (e.g. Chapman et al. 2011; Butterfield et al. 2024; Pillai et al. 2015), and high velocity dispersions of >100 km s $^{-1}$ (e.g. Sormani et al. 2019). Furthermore, the Galactic Center of the Milky Way varies from the Galactic disk environment where temperatures, turbulence, densities, and magnetic field strengths are about an order of magnitude lower (Henshaw et al. 2023). While the conditions in the CMZ are dissimilar to those of the Galactic disk, they are congruent with those found in starburst (Crocker 2012), ultra luminous infrared, and high-red-shift galaxies (Kruijssen & Longmore 2013a), which are known for their high star formation (e.g. Garca-Burillo et al. 2012; Seymour et al. 2008). Despite the CMZ having a similar environment (Kruijssen & Longmore 2013b), it produces stars an or-

der of magnitude below what it should for the amount of dense gas present (Longmore et al. 2013; Immer et al. 2012), generating interest in studying the molecular gas properties and dynamics in the CMZ in recent years.

The CMZ contains roughly $2-6 \times 10^7 M_\odot$ (Dahmen et al. 1998; Ferriere et al. 2007; Battersby et al. 2024a) corresponding to 3-10% of the total molecular gas in the Galaxy (Roman-Duval et al. 2016). This molecular gas is concentrated in molecular clouds of different sizes and densities that can form clumps and cores, within which stars can form under the right conditions. The cool temperature of molecular gas and lack of a permanent electric dipole moment of the most abundant molecule, H $_2$, make it difficult to study MCs using H $_2$. Instead examples of molecular lines used to map MCs include CO (e.g. Bania 1977; Oka et al. 1996, 1998), NH $_3$ (e.g. Purcell et al. 2012), and H $_2$ CO (e.g. Walsh et al. 2011). Other molecules such as HCN or SiO can be used to trace the densest parts of these clouds which can be shocked (Martın-Pintado et al. 1997). Furthermore, radio and submillimeter telescopes have also helped to map the distribution of the densities of these MCs in

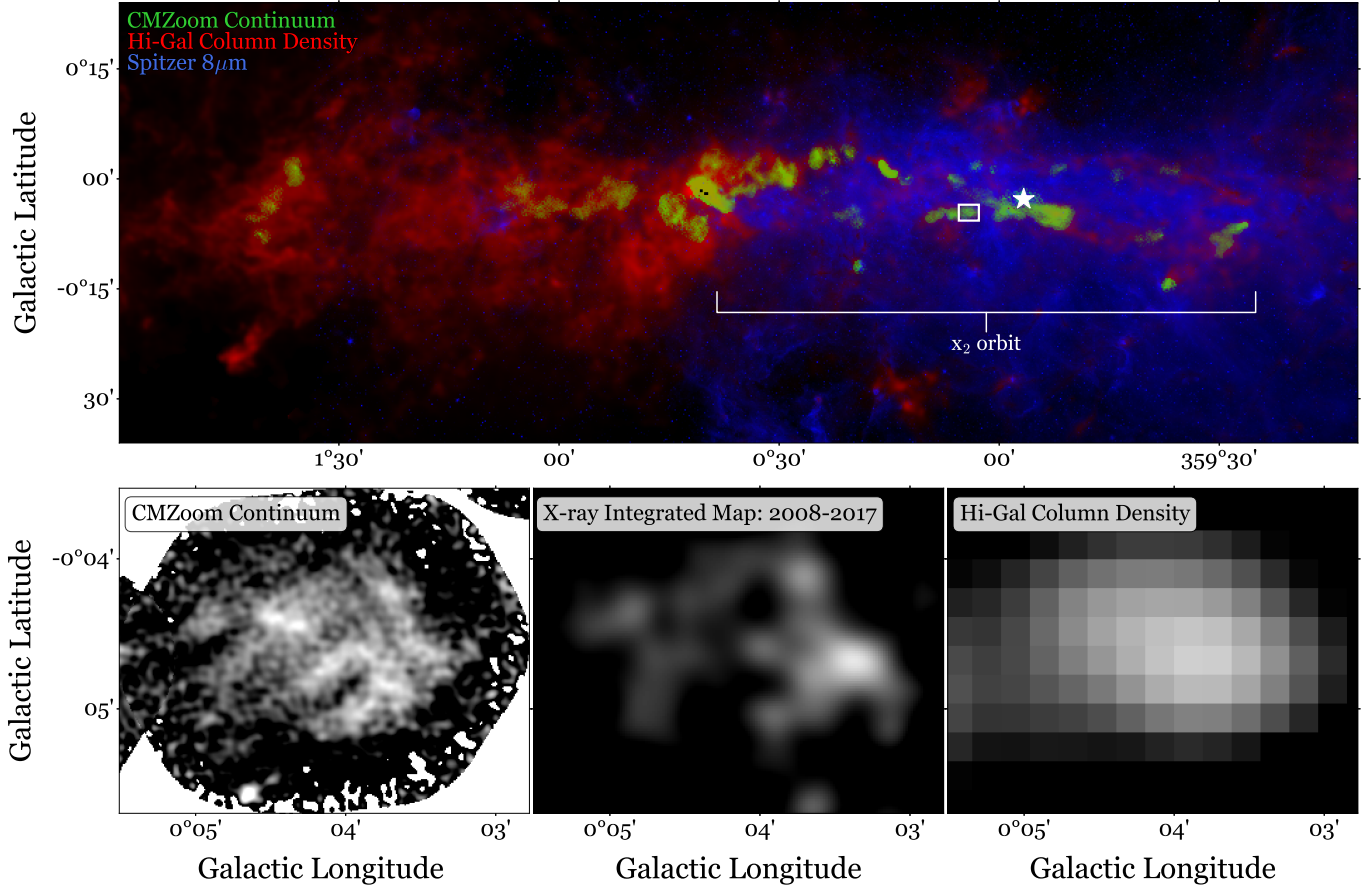


Figure 1. Top: RGB image of the Central Molecular Zone (Red: Hi-Gal Column Density, Blue: Spitzer $8 \mu\text{m}$, Green: CMZoom Continuum). The white star represents the position of Sgr A* while the white rectangle shows the position of the Stone MC. The bottom three panels represent the data used for analysis in this paper. From left to right: H_2CO integrated map observed by the Submillimeter Array, Submillimeter Array CMZoom continuum, *Chandra* X-ray integrated emission from 2008–2017, and the Herschel Hi-Gal Column density of the Stone MC. Scale bars are located on the bottom left of each panel while the beam sizes

projection (e.g. Sofue & Handa 1984; Novak et al. 2003; Battersby et al. 2020).

Previous studies show that the molecular gas flows along the galactic bar and into the inner CMZ (Sormani & Barnes 2019; Hatchfield et al. 2021; McClure-Griffiths et al. 2012; Su et al. 2024) at a distance of approximately 100 pc with a semimajor axis perpendicular to the bar (Binney et al. 1991; Sormani et al. 2015). Most of the gas in the CMZ, as well as the dense MCs, lie on an approximately elliptical orbit, called the Milky Way’s inner x_2 orbit, surrounding Sgr A*. The exact orbital model is widely debated but current models include a closed ellipse, an open stream, and two spiral arms (Sofue 1995; Kruijssen et al. 2015; Molinari et al. 2011). The most recent literature show that the best-fit orbital model is an improved version of the Kruijssen et al. (2015) ellipse model (Walker et al. 2024; Lipman et al. 2024). Only by uncovering the 3D distribution of MCs and gas in the

CMZ can we understand the connection between gas inflow, star formation, black hole feeding, and outflow.

The individual 3D structure of MCs are hard to accurately model in the CMZ (Beaumont et al. 2013). This is partly due to the fact that extreme extinction in the CMZ, ($A_V \gtrsim 30$ mag, $A_{K_s} \gtrsim 2.5$ mag, Nishiyama et al. 2008; Schödel et al. 2010), along with crowding hampers observations and extinction methods of the CMZ. Previous studies have probed the 3D structure of MCs locally with distances up to 2.5 kpc (Dharmawardena et al. 2023; Zucker et al. 2021). These methods include using *GAIA* astrometric measurements coupled with dust extinction (Foley et al. 2023) or 3D position-position-velocity (PPV) maps using the radial velocity of CO combined with dust mapping techniques (Zucker et al. 2021; Dharmawardena et al. 2023). In this paper, we introduce a method to map out individual MCs in 3D using X-ray echoes that propagate throughout the CMZ and physically interact with MCs.

The X-ray emission from the Galactic center includes a soft plasma around $1\text{ kT}\sim 1\text{ keV}$ (Ponti et al. 2015), X-ray emission through point sources (e.g. Wang et al. 2002; Munro et al. 2003, 2009; Zhu et al. 2018), extended but not diffuse features (e.g. Zhang et al. 2020; Churazov et al. 2024), a hot and diffuse emission revealed by 6.7 keV Fe XXV (e.g. Park et al. 2004; Anastasopoulou et al. 2023; Koyama 2018), and a non-thermal component including a strong $6.4\text{ keV Fe K-}\alpha$ line that correlates with molecular gas (e.g. Murakami et al. 2000; Sunyaev et al. 1993; Koyama et al. 1996; Terrier et al. 2018). The energetics, time-variability, spectral shape and the polarization properties of the latter component are all compatible with the $\text{Fe K-}\alpha$ line being due to the past X-ray emission of Sgr A* (e.g. Terrier et al. 2010; Ponti et al. 2010; Clavel et al. 2013; Terrier et al. 2018; Marin et al. 2023). This past signal is propagating away from the supermassive black hole and interacts with molecular clouds creating a continuum emission due to X-ray scattering, that is absorbed at low energy. It also creates fluorescent emission lines, including the $\text{Fe K}\alpha$ line that dominates the spectrum (Sunyaev & Churazov 1998). Furthermore, the flux of this fluorescent line is proportional to both the luminosity of the past event and the column density of the illuminated material. The X-ray monitoring of these clouds over the past ~ 25 years (e.g. Clavel et al. 2013; Churazov et al. 2017; Chuard et al. 2018; Marin et al. 2023; Sofue 2000; Predehl et al. 2020) provides a unique opportunity to construct the 3D structure of MCs in the CMZ using the time lags of each X-ray observation as the third axis.

This paper is the second in a series to model the 3D structure of MCs in the CMZ using X-ray tomography. Brunner et al. (submitted) introduced this method for the Sticks cloud located at $(l, b) = (0.105^\circ, -0.080^\circ)$. In this paper, we focus on the adjacent Stone cloud located at $(l, b) = (0.068^\circ, -0.076^\circ)$ as seen in Fig. 1. The Stone cloud is $3.0\times 10^4 M_\odot$ with a radius of 1.9 parsecs (Battersby et al. 2024b) and has a star formation rate of $2.2\pm 1.3\times 10^{-10} M_\odot$ per year (Hatchfield et al. 2024). Similar to the Sticks MC, the Stone MC has been observed by X-ray observatories such as *Chandra* and *XMM-Newton* which has been studied in recent literature (e.g. Koyama 2018; Ponti et al. 2010; Clavel et al. 2013; Capelli et al. 2012). In this study we use X-ray emission from the Stone MC to construct a 3D visualization of the MC while characterizing its 3D structure. Section 2 gives an overview of the data used in this study while Section 3 describes the methods used to disentangle the 3D structure of the Stone cloud and estimate its density profile by comparing with continuum and spectral line submillimeter emission. In Section 4

we provide a discussion on the new insights gained from this method and the shortcomings that it may possess. In Section 5 we summarize the key takeaways of this method.

2. DATA

2.1. X-ray echoes

The X-ray observations of the Stone cloud were obtained using archival ACIS-I data from the *Chandra X-ray Observatory* covering the period 1999–2017. The data were reduced using CIAO v4.8, and following the method described in Clavel et al. (2013), to obtain maps of the continuum subtracted 6.4 keV emission line¹. To achieve a higher signal to noise ratio, the data are merged into one mosaic per year, except for 2012 and 2014 where no ACIS-I observation is available. These $\text{Fe K}\alpha$ mosaics tracing the X-ray echoes propagating in the Stone cloud have deep exposures in 2002, 2004, 2008, 2009, 2011, 2015, 2016 and 2017 with total clean exposures above 100 ks, and shallower ones ranging from 25 ks (in 2003) to 80–90 ks (in 2010 and 2013). Subsequent observations show a decreasing trend Khabibullin et al. (2022). Therefore only the 2008–2017 years are used in the subsequent analysis of this paper.

2.2. Hi-GAL column density map

The CMZ was observed with the *Herschel Space Telescope* through the Herschel infrared Galactic Plane (Hi-GAL) survey (Molinari et al. 2010, 2016) covering the Galactic plane at $-l\leq 70^\circ$ and $-b\leq 1^\circ$. The Spectral and Photometric Imaging Receiver (SPIRE; Griffin et al. 2010) and the Photodetector Array Camera and Spectrometer (PACS; Poglitsch et al. 2010) on *Herschel* observed the Galactic center at wavelengths of 70, 160, 250, 350, and $500\ \mu\text{m}$ with beam sizes of $6''$, $12''$, $18''$, $25''$, and $36''$ respectively. The column densities of MCs in this survey were derived by subtracting the cirrus emission from the Galactic center and performing modified black-body fits to the cold dust component of the *Herschel* data. We refer the reader to Battersby et al. (2011, 2024a) for a complete explanation of this method.

2.3. CMZoom Survey

The CMZoom survey (Battersby et al. 2020) is a large scale survey conducted with the Submillimeter Array over 550 hours covering 350 arcmin^2 of the Milky Way's

¹ In addition to the observations listed in Clavel et al. (2013), we used *Chandra* Observation IDs (in chronological order): 13017, 13016, 14942, 14941, 14897, 17239, 17236, 18852, 17237, 17240, 17241, 17238, 20118, 20807, 20808, obtained in 2011, 2013 and 2015–2017.

CMZ. The CMZoom survey mapped 1.3 mm dust continuum and spectral line emission in the CMZ above a molecular hydrogen column density of 10^{23} cm^{-2} . At these wavelengths we are most sensitive to cold, dense, star-forming gas and dust. This data has a resolution of $3''$, or 0.1 pc, at a Galactic Center distance of 8.2 kpc (GRAVITY Collaboration et al. 2019) allowing us to study MCs in great detail. The dust continuum map for the Stone MC can be found in Fig. 1.

In addition to a continuum map, we use several molecular tracers to map the Stone Cloud. These include $\text{H}_2\text{CO } 3(0,3)-2(0,2)$ at 218.2 GHz and $\text{H}_2\text{CO } 3(2,2)-2(2,1)$ at 218.5 GHz which map the dense gas, while the $\text{SiO } (5-4)$ transition at 217.1 GHz is used to map protostellar outflows and shocks (Callanan et al. 2023).

3. METHODS & RESULTS

3.1. Assumptions based on the Geometry of X-ray Echoes

The X-ray emission of the Stone MC has been interpreted as an echo from a past outburst from Sgr A* which occurred before the advent of X-ray astronomy and lasted at most 1 or 2 years (Ponti et al. 2010; Clavel et al. 2013; Churazov et al. 2017). In this context, at a given time t after the event, the material seen as illuminated by an observer on Earth follows the paraboloid:

$$z(t) = \frac{1}{2} \left(ct - \frac{d_p^2}{ct} \right), \quad (1)$$

where c is the speed of light, $z(t)$ is the line-of-sight distance of the illuminated material, and d_p is the distance between Sgr A* and the MC in projection (Sunyaev & Churazov 1998). The time that light travels to the observer when interacting with a MC will include a time delay for the specific distance the light travels from Sgr A* to the MC (d_p). To take into account the time delay we can write the total time light travels as $\left(ct - \frac{d_p^2}{ct} \right)$. In addition, the factor of $\frac{1}{2}$ represents the two separate paths light takes to reach the observer, i.e. light travels from the source to material and then from the material to the observer. Therefore, equation (1) can be used to link the 3D geometry of the X-ray emission to the age of the Sgr A*'s past event, which is however poorly constrained. Recent estimations from various regions within the CMZ gave ages ranging from one to a few centuries (Clavel et al. 2013; Churazov et al. 2017; Chuard et al. 2018; Marin et al. 2023). Due to projection effects, the distance between two parabolas separated by one year is larger than a light-year for MC having a negative line-

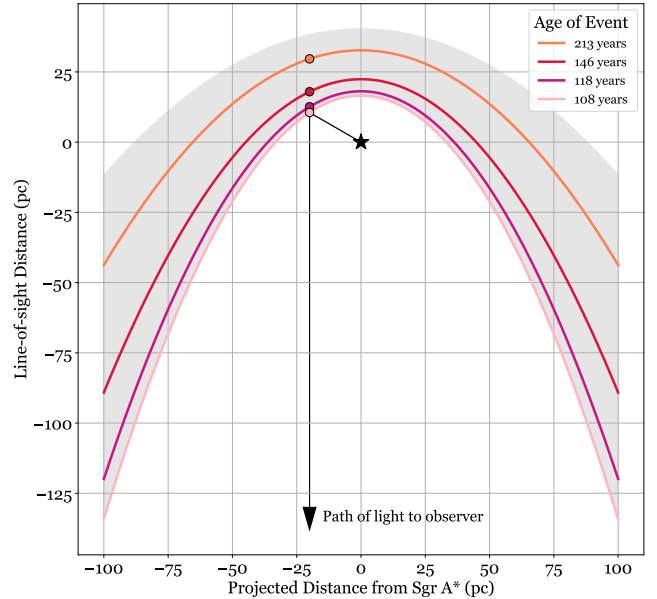


Figure 2. Top-down view of the CMZ with Sgr A* plotted at (0, 0) and parabolas following Eq. 1. We consider scenarios where the X-ray flare propagated 108, 118, 146, and 213 years ago (Clavel et al. 2013; Churazov et al. 2017; Chuard et al. 2018; Marin et al. 2023) (as of January 1st, 2008) with errors (shaded gray area). The circles correspond to the line-of-sight distance of the Stone MC given the different ages of the events.

of-sight distance and smaller than a light-year for MC having a positive line-of-sight distance.

In this paper we assume an age for the X-ray flare by using the calculated ages from previous studies (Clavel et al. 2013; Churazov et al. 2017; Chuard et al. 2018; Marin et al. 2023). Fig. 2 shows all the possible scenarios for the X-ray flare event given different age estimates using 2008 as the reference year with errors stemming from the literature values. The median of this sample is 132 years while the mean is 140 years with a standard deviation of 39.72 years. Although the median is often used to represent the average of a sample, we use the mean value for this work because of the small sample size available. Assuming that the age of the X-ray flare event was 140 years ago, the line-of-sight distance can be calculated to $\sim 17_{-6}^{+21}$ pc behind Sgr A* by using Eq. 1. Errors for the line-of-sight calculation come from the errors in previous literature which are also shown in Fig. 2. Other studies suggest that the Stone MC (commonly referred to as a section or multiple sections in the Bridge region) is 16.3–21.6 pc (Capelli et al. 2012), ~ 10 pc (Churazov et al. 2017), and 18 pc (Ponti et al. 2010) pc behind Sgr A*. All line-of-sight distance estimates in previous literature are based off different assumptions in the age of the event and definitions of this region.

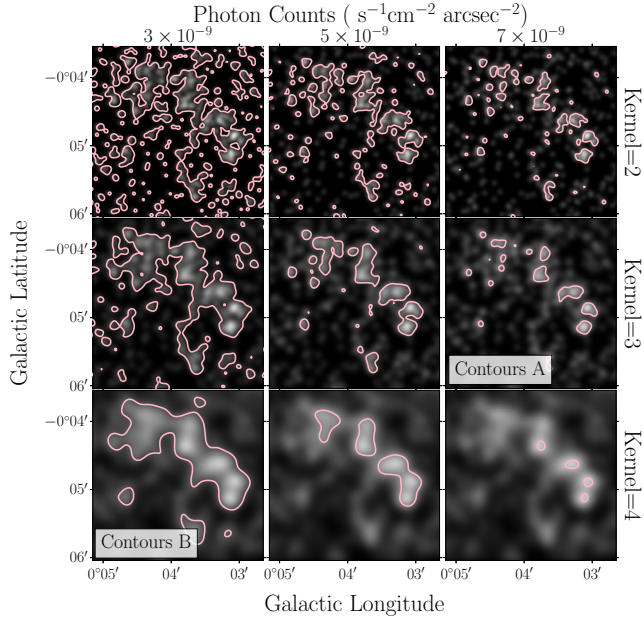


Figure 3. We investigate possible X-ray smoothing kernels and contour levels in order to select the ones that best represented the overall structure seen in X-rays. This figure shows X-ray data of the Stone (left) MCs collected in 2010. Shown from top to bottom are increasing numbers of kernels used for smoothing. From left to right, an increasing flux level of contours are drawn. In this work we use the panels the middle right and bottom left panels (Contours A and B respectively) to show the overall structure and the densest parts of the Stone MC.

3.2. The structure of the Stone MC as seen by X-ray echoes

Chandra X-ray Observatory, like other X-ray observatories, measure X-rays per photon on their detector along with their energies and spatial information. Noise in an image can be introduced due to the natural low photon count rates, stochastic nature of X-ray emission, and noise introduced when the photons hit the detector. These random fluctuations from an object can create a grainy background, concealing the origin of the X-ray emission. To make sure we are isolating the X-ray emission from the MC, we minimize background noise in the continuum subtracted 6.4 keV maps by smoothing yearly mosaics using a Gaussian smoothing kernel. Averaging the pixel values of the photon counts within neighboring pixels attenuates noise, increasing the signal-to-noise ratio. However, there is a delicate balance between smoothing just enough to minimize noise and reveal astronomical objects and smoothing too much which can remove important smaller features.

Fig. 3 shows different smoothing kernels considered for the X-ray data with different levels of flux drawn as

contours. If we use a higher smoothing kernel, less noise is introduced leading to a higher signal-to-noise ratio, however the resolution of the data decreases.

To show the overall structure with minimum noise and high resolved areas, we use two combinations of smoothing and flux levels (see Figs. 3 and 4) which are used in part one of this series (Brunker et al., submitted). We use a Gaussian smoothing kernel of four and contour level of 3×10^{-9} ph cm $^{-2}$ s $^{-1}$ arcsec $^{-2}$ to trace the overall shape of the Sticks MC and a smoothing kernel of three and contour level of 7×10^{-9} ph cm $^{-2}$ s $^{-1}$ arcsec $^{-2}$ (hereafter referred to as Contours A and Contours B respectively) to identify highly resolved high flux areas. To have a consistent comparison between the Stone MC, the Sticks MC, and any other MC we choose to construct moving forward, we will use the same contour levels and smoothing kernel. We see that the X-ray emission is prominent in years 2008–2013 with smaller pockets of higher X-ray emission embedded in the thicker contours. However, after 2013 the MC lacks a clear structure and the higher X-ray emission is lost, indicating that the light front has left the densest part of the cloud.

In order to create 3D models of MCs, we use the X-ray contours drawn in Fig. 4 and the assumptions made in Section 3.1 to convert the time lags to physical distance. We then use the physical distance as the third axis in creating the Stone cloud’s 3D structure (see Fig. 5). We can see that there is a cohesive structure between the years 2008 to 2013 while later years show smaller areas of X-ray emission that don’t match the pattern seen in earlier years. Furthermore, we can estimate the lower limit of the extent to be $1.66_{-0.20}^{+0.18}$ pc based off of the standard deviations of the age of the event and Eq. 1 described in Section 3.1.

3.3. Spectral line dendrograms

We use a hierarchical structure algorithm, *astrodendro*, to identify structures within the H $_2$ CO 3(0,3)–2(0,2) at 218.2 GHz for the Stone MC. A dendrogram consists of trunks, i.e. structures with no parent structures and with the lowest emission, and branches, which split into multiple sub-structures called leaves. The leaves of a dendrogram have no additional sub-structure to them and are thus the highest level of structure with the brightest emission.

The dendrogram algorithm is used to tease out the structures located within the Stone MC of the H $_2$ CO (218.2 GHz) data cube where each channel has a width of 1.1 km s $^{-1}$. For each velocity spanning from 30.2 km s $^{-1}$ –73.8 km s $^{-1}$ (40 channels in total) the median and standard deviation of the background are calculated. Specification of a dendrogram requires three param-

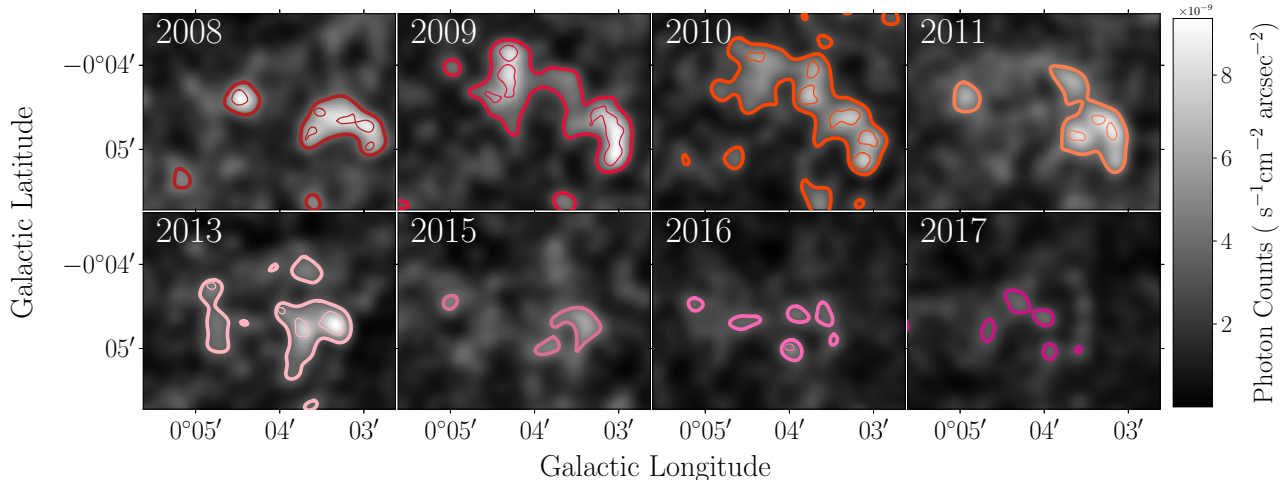


Figure 4. X-ray data collected from 2008–2017 show the most significant 6.4 keV emission in the vicinity of the cloud. The X-ray emission is plotted in gray scale, smoothed with a Gaussian kernel of 4. Over plotted are the Contours A in bold and Contours B in thin lines.

ters: the minimum value considered to be a structure, minimum delta or the difference of the peak flux of one structure and the structure that branches from it, and minimum number of pixels that constitutes a structure as a separate entity. The minimum delta value is 3σ above the mean value while the minimum delta parameter is set to 8σ above the mean value. The minimum number of pixels was set to $3'' \times 3''$ which is equivalent to the beam size of the CMZoom survey. For more information about the beam sizes for different regions of the CMZ, see [Battersby et al. \(2020\)](#).

The algorithm finds 2 trunks, 19 branches, and 21 leaves. The regions with the highest flux, or the leaves, of the dendrogram can be seen in [Figures 6 and 7](#). Each leaf structure has a corresponding index number for identification which is labeled in [Fig. 6](#) and shown in [Table 1](#) (except leaf 10 which is both a trunk and a leaf). The index IDs of each structure in the dendrogram have no physical meaning but are randomly assigned by the algorithm. For each of the leaves in [Table 1](#) the Δv is identified as the total velocity extent of each structure and the \bar{v} are the mean values of the total velocity extent. The leaves are the grouped together from $30.2 \text{ km s}^{-1} - 40 \text{ km s}^{-1}$, $40 \text{ km s}^{-1} - 50 \text{ km s}^{-1}$, and $50 \text{ km s}^{-1} - 63.8 \text{ km s}^{-1}$ based off of the mean central velocities of each in [Table 1](#) and are shown in [Fig. 6](#). In addition, the X-ray years are also split into these three groups based on their mean \bar{v} which are calculated by calculating the mean \bar{v} of all the structures that correspond to it. If multiple years are grouped within the same velocity range, the outlines of their corresponding contours (Contours A) are added together.

We then match each leaf with an X-ray year by overlaying the structures found in each velocity and com-

paring their positions to the area covered by the X-ray echoes (see [Fig. 7](#)). In addition, we use the central velocities found in [Table 1](#) to further constrain the groupings. For example, if a leaf is in the same projected position as two separate X-ray years, we favor the year in which other leaves have similar velocities. This way we are able to group structures together in PPV space and their projected area. All leaves except 6, 21 and 25, which are shown in gray scale in [Fig. 7](#) are given a corresponding X-ray year.

The regions with lower flux, trunks and branches, can be seen in [Fig. 8](#) where each structure is integrated from the velocity extent of the MC ($30.2 \text{ km s}^{-1} - 73.8 \text{ km s}^{-1}$). We refer the reader to [Section 3.4](#) for an in depth analysis.

3.4. Integrated Structure Maps

We transform 3D information in the form of X-ray echoes and spectral line data cubes into 2D images to compare them to data sets that only observe 2D structure (such as column densities).

First, we use two different methods to create integrated X-ray contours shown in [Fig. 8](#). Integrated X-ray contours are created emphasizing the:

1. Maximum X-ray brightness per year where lower level contours (Contour A) shown in [Figs. 4 and 5](#) (with contours less than 15 arcsec omitted) are used. The integrated contour is then drawn from the outline of the individual years added together. This gives more weight to clumps in the MC as they are localized areas that are less dense than the overall MC but still pass the minimum threshold flux.

Table 1. Leaf structures in the dendrogram are matched with the X-ray year contours, showing that the structures in the same year are in similar areas in PPV space. There are only 2 leaves that do not correspond to an X-ray contour (see the ‘Other’ section at bottom). Leaves considered but not included with the groupings are Index 10 because it is both a leaf and a trunk and Index 6 because of its large average velocity. From left to right: X-ray years, the index of the corresponding dendrogram structure (only the leaves are used for this analysis) Δv , average velocity for each structure, and the average velocity of all structures for their corresponding year. All values in the table have rounding errors of $\pm 0.1 \text{ km s}^{-1}$.

Year	Index	$\Delta v \text{ (km s}^{-1}\text{)}$	$\bar{v} \text{ (km s}^{-1}\text{)}$	Mean $\bar{v} \text{ (km s}^{-1}\text{)}$	Standard Deviation	Standard Error
2008	27	12.3	45.4	40.0	3.5	1.4
	18	14.6	37.5			
	31	10.0	43.1			
	32	15.7	38.1			
	34	5.5	40.9			
2009	19	5.4	42.1	38.5	2.6	1.5
	18	14.6	37.5			
	39	8.9	35.9			
2010	17	15.7	38.1	37.0	1.2	0.7
	18	14.6	37.5			
	38	10.1	35.3			
2011	31	10.0	43.1	40.6	2.5	1.7
	36	15.7	38.1			
2013	26	10.1	48.7	43.8	3.9	2.0
	15	12.3	45.4			
	31	10.0	43.1			
	33	13.4	38.1			
2015	27	12.3	45.4	40.3	3.6	2.0
	32	15.7	38.1			
	37	14.6	37.5			
2016	30	3.3	47.6	42.8	4.75	3.4
	32	15.7	38.1			
2017	28	3.3	58.8	59.7	0.8	0.6
	6	13.3	57.2			
Other	21	13.4	57.1	54.1	4.3	3.1
	25	15.9	48.0			
	6	13.3	57.2			

2. Relative X-ray brightness over all years where the X-ray data is smoothed with a kernel of 4 and all the years between 2008 and 2017 are added together. The integrated contour is then drawn based off of this map at $1.2 \times 10^{-8} \text{ ph cm}^{-2} \text{ s}^{-1} \text{ arcsec}^{-2}$. Unlike the first method, this method gives more weight to extended features in the X-ray data.

Additionally, we produce an integrated image with additional spectral lines of different molecules. We use $\text{H}_2\text{CO } 3(0,3)-2(0,2)$, $\text{H}_2\text{CO } 3(2,2)-2(2,1)$, and $\text{SiO } (5-4)$ to trace the dense molecular gas in the Stone MC. Each is integrated over the velocity range of the cloud ($30.2 \text{ km s}^{-1}-73.8 \text{ km s}^{-1}$) and assigned a color which is then overlaid in a single plot (see Fig. 9).

Fig. 8 compares the integrated X-ray contours with other data seen in the line-of-sight including the CM-Zoom continuum and Herschel Hi-Gal column densities and the branches and leaves from the dendrogram. We see that the maximum integrated contour does not trace the densest structures but instead encompasses the less dense areas of the MC. Conversely, the relative integrated contour is able to trace the outer arc and majority of the inner arc, but fails to trace a small part of the brightest point (top left circular area) of the MC. Meanwhile, both X-ray integrated contours fail to trace over the lower center structures (the leftmost parts of the inner arc). On the other hand, Fig. 9 shows that all three spectral lines are in agreement with each other and the structure of the Stone MC seen in the submillime-

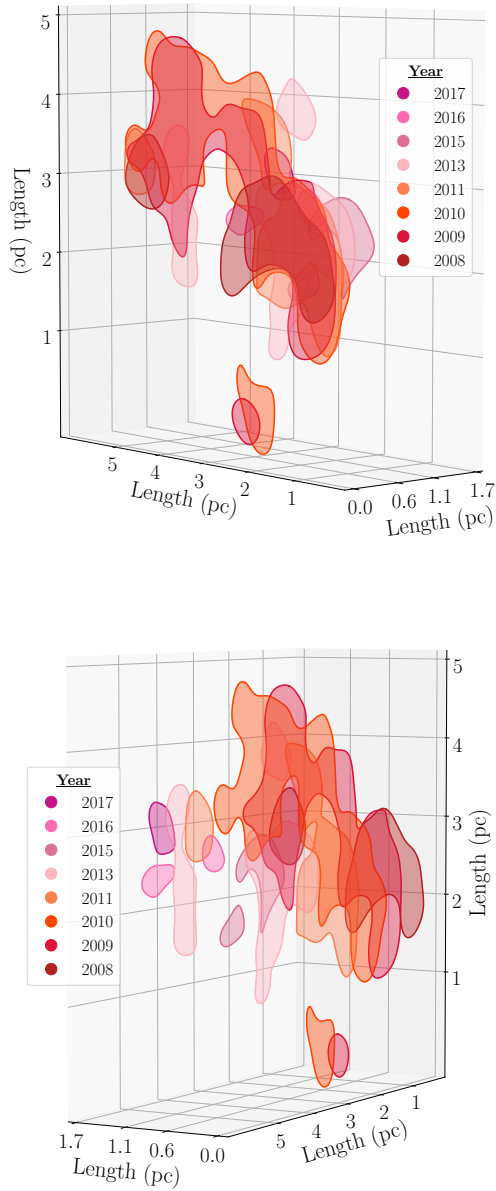


Figure 5. Using Eq. 1 and assuming an X-ray flare event ~ 140.6 years ago (See Section 3.1) where $d_{los} = 17$ pc, we are able to create a 3D model of the Stone MC with Contours A. Structures that were less than 15 arcsec wide were omitted from the plot to omit background fluctuations.

ter continuum (see Fig. 1), showing that it is a reliable tracer of dense gas in the Stone MC.

3.5. Calculating localized densities

For further analysis of the 3D properties of the Stone MC we calculate the density of material for each relevant year. We make the assumption that the relationship between the X-ray emission and Herschel column den-

sities are linearly proportional however, the position of the peak flux in the relative X-ray brightness integrated maps (as described in Section 3.4) and the Herschel column density differ by about $30''$ (for reference, the beam size for Herschel 350 μm emission is $35''$). Since the X-ray echoes are not measured continuously, this could indicate that the brightest parts of the MC are missed by *Chandra*. Although this is an issue for our assumption, we move forward with the calculation, hoping future studies can improve this calculation.

In order to create localized densities for each year of the cloud, we identify the peak X-ray intensity of the integrated X-ray flux (see Fig. 8) and the peak column density from Herschel. We then divide the peak flux in the column density by the peak X-ray flux to find a density normalization factor of $1.23 \times 10^{31} \text{ s arcsec}^{-2}$. This normalization factor is then multiplied by the X-ray flux in each observation to obtain a localized density for every pixel in each X-ray year. Fig. 10 shows that years 2008, 2009, and 2010 contribute the highest densities at around $1 \times 10^{23} \text{ cm}^{-2}$. Moreover there are smaller dense regions illuminated in 2009 and 2010 which then become less dense in 2011 and 2013, disappearing after 2013. Since the CMZoom continuum integrates all of the dust along the line-of-sight while the X-ray emission only covers the emission observed at a certain time, the continuum is a fixed number and the X-ray emission is a lower bound. If we were to observe more X-ray emission, then the normalization factor would only decrease, meaning that our density calculations for each year is an upper limit.

4. DISCUSSION

4.1. The spectral line counterparts of the X-ray echoes

Typically, doppler velocities can not be assumed to follow linear time such as the X-ray flux, especially if there are other factors such as turbulence or star formation that could skew the velocity ranges detected. By following each substructure through different velocities, we show that most of the lower emission X-ray contours (Contours A) cover the leaves from the dendrogram. While some of these leaves are completely covered by the X-ray emission, other leaves are only partially covered, while very few (about 2 leaves) are not covered by the X-ray data at all. The velocity dispersion for each leaf in Table 1 shows a large range from as wide as 15.7 km s^{-1} to as low as 1.2 km s^{-1} . This means that some structures in the Stone MC are extended while structures with small velocity dispersions can be described as small clumps of dense gas. In addition, we find average velocities for each year along with its standard deviation and error. The standard deviation show a small spread

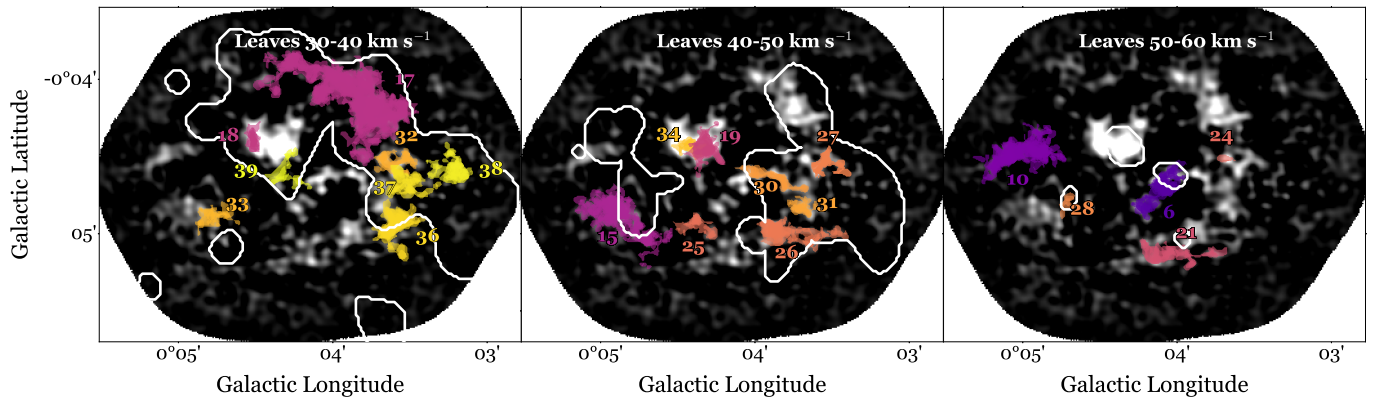


Figure 6. Grouping structures with similar velocity ranges reveal an overall trend in the leaves seen in PPV space. Left panel: Leaf indices 17, 18, 32, 33, 36, 37, 38 and 39. Center panel: Leaf indices 15, 19, 25, 26, 27, 30, 31, 34. Right panel: Leaf indices 6, 10, 21, 24, and 28. Integrated X-ray contours are created based on the mean \bar{v} in Table 1 and shown as white contours in each panel (Left: 2008, 2009, 2010. Center: 2011, 2013, 2015, 2016. Right: 2017.)

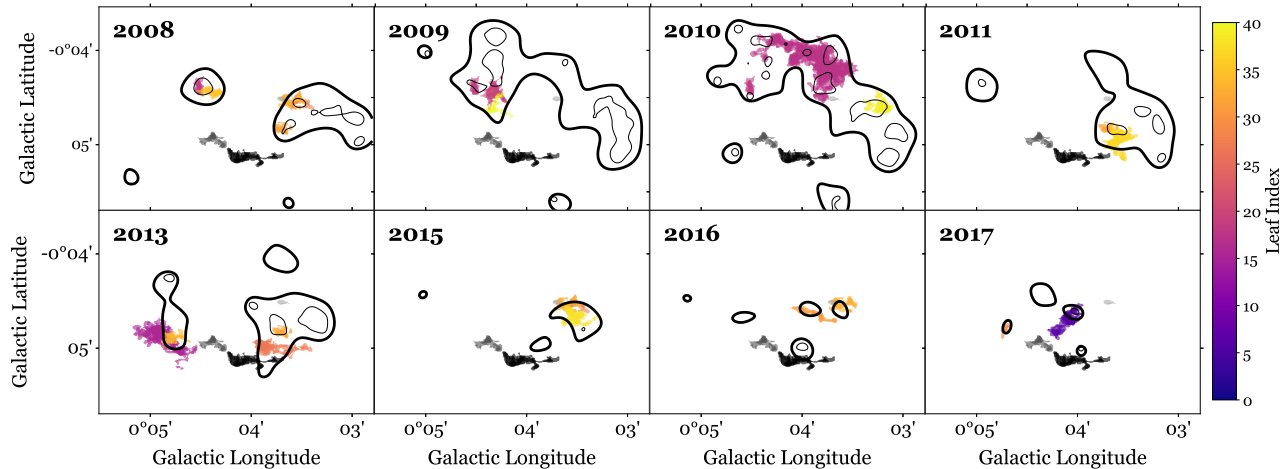


Figure 7. Dendrogram leaves of the H_2CO spectral line show good correspondence with X-ray contours. Structures colored from yellow to purple represent different structures that are correlated while the structures in gray-scale are unmatched with a particular feature in the X-ray. All dendrogram structures are seen in the H_2CO spectral line within 30.2 km s^{-1} to 73.8 km s^{-1} . Contours A are drawn in bold while Contours B are drawn thinner. For detailed information about the overlaid datasets and the velocity ranges for each dendrogram structure, see Table 1.

of velocities ($\leq 5 \text{ km s}^{-1}$) for all years. Indices 27, 18, 31, and 32 have very wide velocity spreads ($12.3, 14.6, 10.0, 15.7 \text{ km s}^{-1}$ respectively).

In addition, the branches and trunks of the dendrogram are compared with the X-ray integrated contours in Fig. 8. Here, we can see that both integrated contours match the overall shape of the dendrogram except in the middle where the top part of the inner arc is not covered by X-rays. For the far right area, this mismatch can be attributed to the limited field of view of the CMZoom survey which is less sensitive to emission in the outer areas of the circle. Moreover, when comparing both integrated X-ray contours with the Hi-Gal column density which has a wider field of view, the X-ray contours encompass the cloud completely.

4.2. Do certain structures occupy similar volumes in space?

We analyze each leaf's location in PPV and projected space, to group leaves and X-ray echoes together. Interestingly, leaves in the 30.2 km s^{-1} – 40 km s^{-1} range are located in two separate areas: the larger arc (on the top and right side of the image) and small parts of the left side. Leaves in the 40 km s^{-1} – 50 km s^{-1} range begin to fill in the right side of the smaller arc (near the middle of the image), the bright circle near the top left, and the outer left areas of the image. Lastly, the leaves in the 40 km s^{-1} – 63.8 km s^{-1} range trace the left most part of the inner arc and the rest of the outer left structures in the image. Furthermore, when looking at the overall trend of all three panels, we see the structures appearing

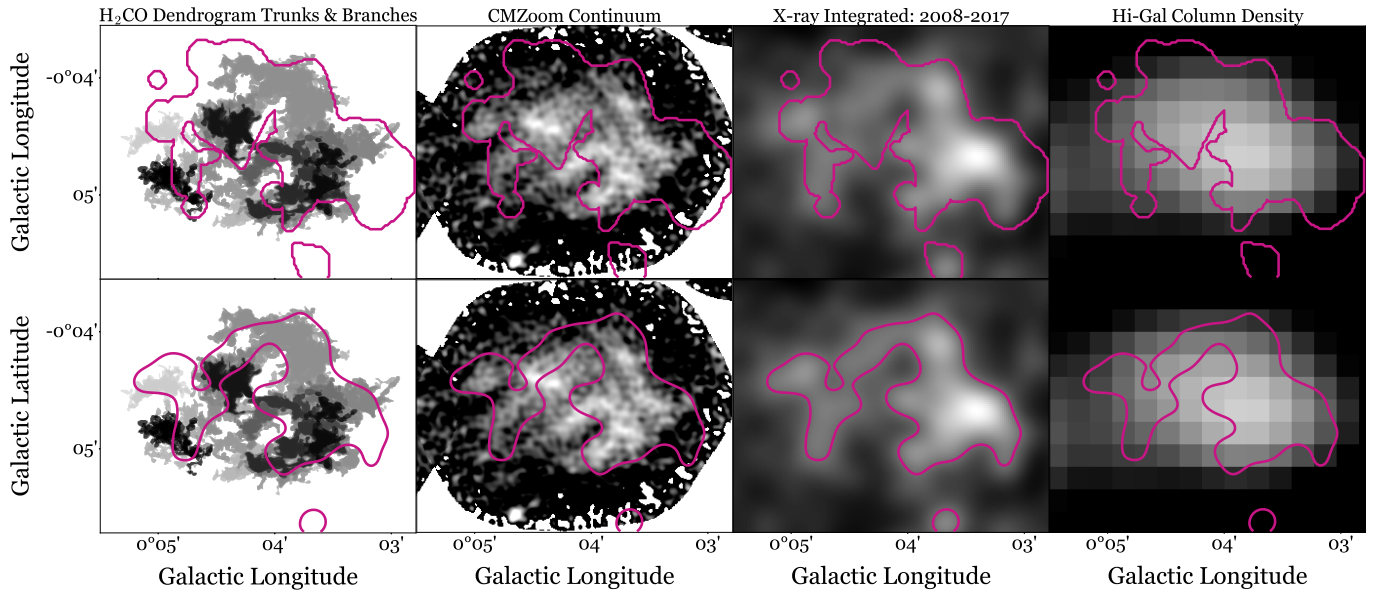


Figure 8. Integrated X-ray contours highlight the overall structure of the Stone MC. Top row: Maximum X-ray brightness contour, Bottom row: Relative X-ray brightness contour (see Section 3.4 for more details). From left to right: Branches and leaves of the H_2CO (218.2 GHz) dendrogram colored by structure ID, CMZoom 1.3 mm continuum, X-ray 6.4 keV emission integrated from 2008–2017, and Hi-Gal column density.

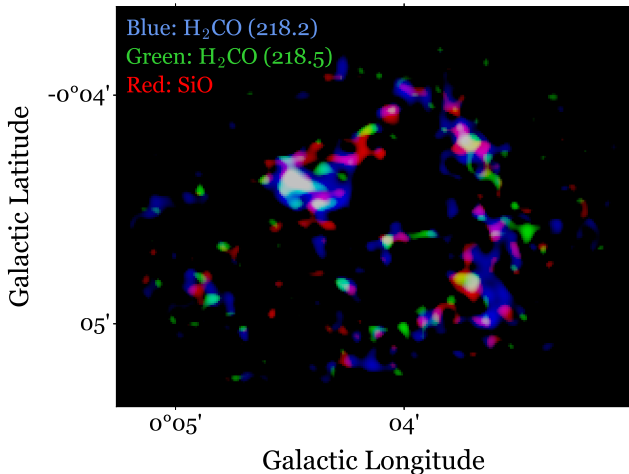


Figure 9. Spectral lines integrated reveal the 2D shape of the Stone MC from our line-of-sight. The spectral lines used were H_2CO 3(0,3)–2(0,2), H_2CO 3(2,2)–2(2,1), and SiO (5–4) plotted in blue, green, and red respectively.

from right to left as the doppler velocities increase. It is worth noting that leaf 2 (can be seen in panel 3 of Fig. 6 as the purple leftmost structure) is a leaf and a branch, having no connection to the other leaves in sample.

Similarly, while not perfect, the X-ray echoes have a similar trend. The emission that reaches the observer

first (in 2008, 2009, 2010) outline the larger arc, while the right side of the inner arc and the left side of the image are also highlighted in the years 2011, 2013, 2015, and 2016. Lastly, the structures on the left side of the inner arc and the left side of the image are congruent with the X-ray contours beginning to occupy the center most and left side of the Stone MC in 2017.

4.3. Coverage of the X-ray Echoes

While we see very good overlap between the molecular line data and X-rays, there are some features in the molecular lines that is not seen in the X-rays (such as leaves 21 and 25) while leaf 6 is hard to correlate due to its high central velocity and small projected area. We know from Section 3.3 that the majority of the leaves are clumped within similar velocity ranges and lie over the projected area of the cloud as shown in Figures 7 and 8. Thus, we can assume that these features are missing in the X-ray due to the intermittent nature of X-ray observations. In addition, if we assume that the missing leaves are spherical, we can use the widths of the leaves to compute the upper limit of the duration of the X-ray flare event. We plot the area illuminated by 140-year-old event (as of January 1st, 2008) of different duration that would have been observed by the current dataset (see Fig. 11). For an infinitely short event, the extension of each parabola is driven by the duration of the observations, with larger spacing around 2012 and 2014. If the event lasts more than few months, then the extension of the parabolas are driven by the duration of the event.

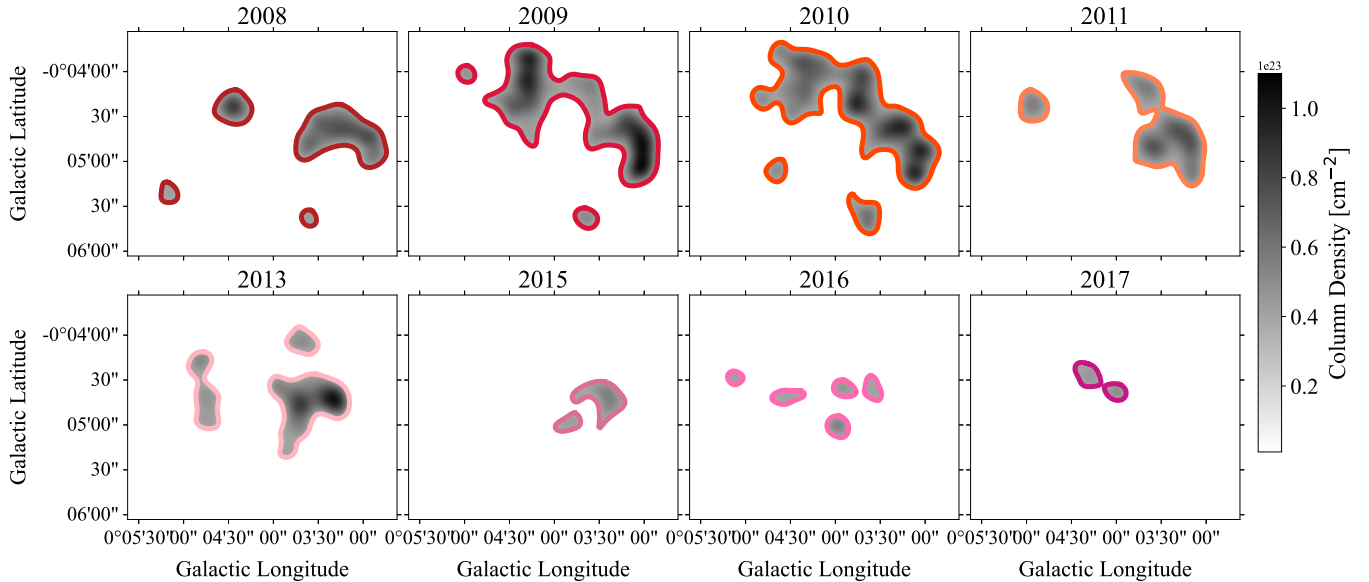


Figure 10. Assuming that the peak in X-ray emission correlate linearly with the peak of submillimeter continuum data from [Battersby et al. \(2020\)](#), we produce localized densities for each slice of the Stone MC. Contours are drawn at 3×10^{-9} $\text{ph cm}^{-2} \text{s}^{-1} \text{arcsec}^{-2}$ from data smoothed with a kernel of four.

The space available for possible missing clumps reduces and completely disappears for events longer than 1.5 years. For an upper limit, where the event that took place $t=140$ years ago, with a duration=0 years, and $d_{proj}=-18$ pc, the maximum extension that could be missed in 2012 and 2014 is ~ 0.28 pc.

We estimate the extension along the line of sight to be equivalent to the diameter of the MC, i.e. ~ 0.3 pc. Therefore, the bulk of X-ray echoes from these clumps could have been missed by the *Chandra* coverage, only if the illuminating event is not much longer than 4–5 months. Such a short duration event is compatible with previous estimations based on X-ray variability studies of this MC (e.g. [Churazov et al. 2017](#); [Clavel et al. 2013](#)).

4.4. Comparing the 3D Structure of the Sticks and Stone MCs

In Paper I of this series ([Brunker et al. submitted](#)), the Sticks MC was modeled using the methods outlined in Section 3 without the dendrogram analysis. Unlike the Stone MC, the features shown in doppler shifted spectral lines and the X-ray echoes progress similarly as velocity and time increases. Furthermore, for the Sticks MC the positions of the peak X-ray integrated flux and the peak column density matched. In contrast, we have no reason to believe that molecular line velocities would necessarily linearly correlate with the physical distance in the Stone MC. In a simple, slowly rotating cloud, the velocity may trace the distance along the line of sight (as it seems to in [Brunker et al, submitted](#)), however, in the presence of feedback from forming stars, localized

turbulence, or other chaotic contribution to the velocity field, this assumption would break down. Dendrogram analysis can provide insight into how structures that are defined in PPV space can be associated with similar physical structures highlighted by the X-rays. Furthermore, the larger X-ray extent as shown by the increase in years of X-ray emission and velocity range extent of the Stone MC indicates the Stone MC may extend further than the Sticks MC in our line-of-sight. In addition the dendrogram analysis revealed its complex substructure by identifying its many clumps which span a wide range of velocity dispersions.

The difference in physical properties of the Stone and Sticks MC should also be taken into consideration. [Callanan et al. \(2023\)](#) has shown that the Stone MC has an abnormally large velocity range for a MC of its size in projection. In particular, factors other than distance can contribute to this range of velocities such as star formation or turbulence within the MC. [Hatchfield et al. \(2024\)](#) estimates the star formation rate of the Stone MC as $2.2 \pm 1.3 \times 10^{-10} M_{\odot}$ while the Sticks cloud does not show signs of current star formation. Thus, a combination of outside factors affecting the spectral line Doppler velocities and the Stone MC's diffuse nature has made it more difficult to model than the Sticks MC.

5. CONCLUSIONS

We have presented a new method using X-ray fluorescence to model MCs in the CMZ from X-ray emission observed over time. The emission is believed to propagate from the supermassive black hole, Sgr A*, af-

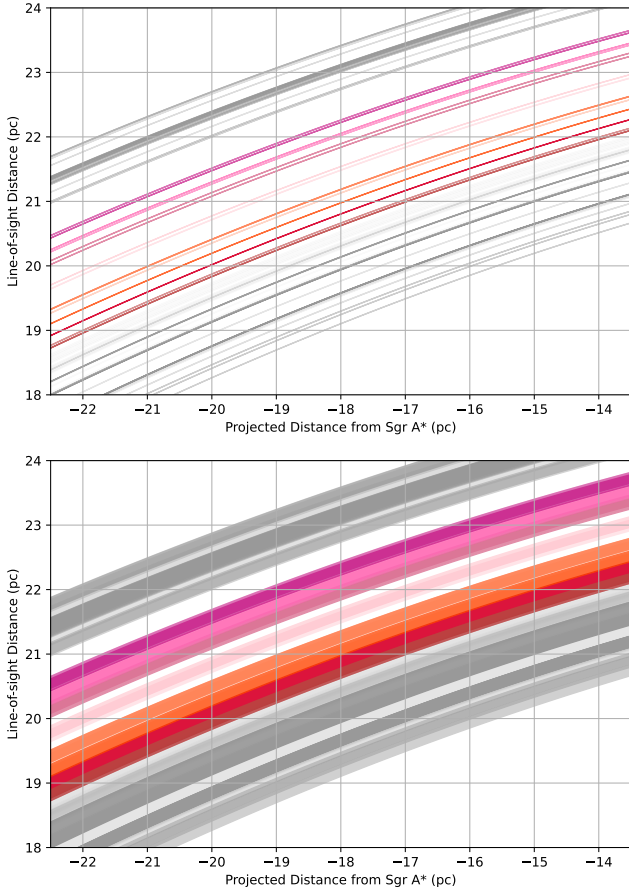


Figure 11. Line-of-sight coverage of existing *Chandra* observations at the projected distance of the Stone cloud, based on their starting date and duration. The parabolas follow equation (1), assuming a 140-year-old event (as of January 1st, 2008) with an infinitely short duration (top) and a one-year duration (bottom). The color indicates the observation year with the same color code as the X-ray contours, and existing observations not studied in this work are marked in gray. Finally, the shading gives an indication of the depth of the observations covering the plane.

ter it accretes material. Over the period of ~ 20 years, *Chandra* X-ray Observatory has detected variable emission from MCs in the CMZ likely due to these X-ray echoes. We use the time lag between each X-ray fluorescence event of the Stone MC as the third axis in creating the 3D model. We have also compared the X-ray emission to various spectral lines from the CMZoom survey (Callanan et al. 2023) and created a dendrogram to analyze the distinct PPV structures in the MC the hierarchical substructure of the MC. From this work:

- We use Gaussian smoothing to improve the signal-to-noise ratio of each X-ray observation and specify two different combinations of kernels used for smoothing along with a flux level used for con-

tours. A higher smoothing kernel with a lower flux level is used to trace the overall shape of the MC while a lower smoothing level with a higher flux is used to identify dense clumps. Furthermore, by assuming the age of the X-ray flare to be 140 years and using Eq. 1, we are able to use the time difference between each observation as a third axis, allowing us to create a 3D model of the Stone MC.

- We identify substructures in the MC using **astrodendro**, a hierarchical structure algorithm, and compare 1) the highest flux structures (leaves) with individual X-ray years and the 2) lowest flux structures (trunks and branches) with the integrated X-ray flux. By identifying the central velocities of each leaf, we are able to match structures to specific X-ray years, combining the PPV areas and the projected areas of each leaf. Detecting X-ray emission that is correlated with the molecular gas indicates that we are seeing X-ray echoes moving through a MC and mapping it over time in 3D. Furthermore, the integrated X-ray emission covers most of the trunks and branches identified, missing an area of ~ 0.3 pc shown in the spectral lines and CMZoom Continuum. On the other hand, the X-ray integrated emission covers the entire area of the MC in projection seen by Herschel, indicating that the missing X-ray data could be responsible for the structures in the H₂CO data not covered by the X-rays.
- By assuming a linear relationship we between column densities and X-ray flux, we find the peak intensities of both data types and calculate their ratio. We use this ratio to compute a pixel-by-pixel column density map for each year of X-ray emission to find localized densities in our line-of-sight.
- By assuming that the missing structures (leaves 21 and 25) seen in spectral lines are spherical clumps, we can constrain the duration of the X-ray flare event. We find that the projected length of the missing clumps are ~ 0.3 pc, meaning the X-ray flare event illuminating the Stone MC could not have lasted more than 5 months.
- The structure of Stone MC is best represented as dense clumps encapsulated by diffuse gas.

We expect to model MCs using X-ray emission for about 5-10 additional MCs in the CMZ. This method can also constrain the line-of-sight distances of MCs as well as constraining the past flaring history of Sgr A*.

ACKNOWLEDGMENTS

DA, CB, and SB gratefully acknowledge funding from the National Aeronautics and Space Administration through the Astrophysics Data Analysis Program under Award “3-D MC: Mapping Circumnuclear Molecular Clouds from X-ray to Radio,” Grant No. 80NSSC22K1125. Additionally, CB gratefully acknowledges funding from National Science Foundation under Award Nos. 2108938, 2206510, and CAREER 2145689. DA acknowledges the Summer Undergraduate Research Fund Award and Research Travel Award from the Office of Undergraduate Research at the University of Connecticut as well as the FAMOUS Travel Grant from the American Astronomical Society. MC acknowledges financial support from the Centre National d’Etudes Spatiales (CNES).

The scientific results reported in this article are based to a significant degree on observations made by the

Chandra X-ray Observatory. This research also made use of data from the Submillimeter Array and the authors wish to recognize and acknowledge the very significant cultural role and reverence that the summit of Maunakea has always had within the indigenous Hawaiian community and we are most fortunate to have had the opportunity to utilize observations from this mountain.

Software: This research has made use of software provided by the Chandra X-ray Center (CXC) in the application package CIAO. This work also made use of Astropy²: a community-developed core Python package and an ecosystem of tools and resources for astronomy (Astropy Collaboration et al. 2013, 2018, 2022), astrodendro, a Python package to compute dendrograms of Astronomical data³, SAO ds9 (Joye & Mandel 2003), and Matplotlib (Hunter 2007).

REFERENCES

- Anastasopoulou, K., Ponti, G., Sormani, M. C., et al. 2023, *A&A*, 671, A55, doi: [10.1051/0004-6361/202245001](https://doi.org/10.1051/0004-6361/202245001)
- Astropy Collaboration, Robitaille, T. P., Tollerud, E. J., et al. 2013, *A&A*, 558, A33, doi: [10.1051/0004-6361/201322068](https://doi.org/10.1051/0004-6361/201322068)
- Astropy Collaboration, Price-Whelan, A. M., Sipőcz, B. M., et al. 2018, *AJ*, 156, 123, doi: [10.3847/1538-3881/aabc4f](https://doi.org/10.3847/1538-3881/aabc4f)
- Astropy Collaboration, Price-Whelan, A. M., Lim, P. L., et al. 2022, *ApJ*, 935, 167, doi: [10.3847/1538-4357/ac7c74](https://doi.org/10.3847/1538-4357/ac7c74)
- Bania, T. M. 1977, *ApJ*, 216, 381, doi: [10.1086/155478](https://doi.org/10.1086/155478)
- Battersby, C., Bally, J., Ginsburg, A., et al. 2011, *A&A*, 535, A128, doi: [10.1051/0004-6361/201116559](https://doi.org/10.1051/0004-6361/201116559)
- Battersby, C., Keto, E., Walker, D., et al. 2020, *ApJS*, 249, 35, doi: [10.3847/1538-4365/aba18e](https://doi.org/10.3847/1538-4365/aba18e)
- Battersby, C., Walker, D. L., Barnes, A., et al. 2024a, arXiv e-prints, arXiv:2410.17334, doi: [10.48550/arXiv.2410.17334](https://doi.org/10.48550/arXiv.2410.17334)
- . 2024b, arXiv e-prints, arXiv:2410.17332, doi: [10.48550/arXiv.2410.17332](https://doi.org/10.48550/arXiv.2410.17332)
- Beaumont, C. N., Offner, S. S. R., Shetty, R., Glover, S. C. O., & Goodman, A. A. 2013, *ApJ*, 777, 173, doi: [10.1088/0004-637X/777/2/173](https://doi.org/10.1088/0004-637X/777/2/173)
- Binney, J., Gerhard, O. E., Stark, A. A., Bally, J., & Uchida, K. I. 1991, *MNRAS*, 252, 210, doi: [10.1093/mnras/252.2.210](https://doi.org/10.1093/mnras/252.2.210)
- Butterfield, N. O., Chuss, D. T., Guerra, J. A., et al. 2024, *ApJ*, 963, 130, doi: [10.3847/1538-4357/ad12b9](https://doi.org/10.3847/1538-4357/ad12b9)
- Callanan, D., Longmore, S. N., Battersby, C., et al. 2023, *MNRAS*, 520, 4760, doi: [10.1093/mnras/stad388](https://doi.org/10.1093/mnras/stad388)
- Capelli, R., Warwick, R. S., Porquet, D., Gillessen, S., & Predehl, P. 2012, *A&A*, 545, A35, doi: [10.1051/0004-6361/201219544](https://doi.org/10.1051/0004-6361/201219544)
- Chapman, N. L., Goldsmith, P. F., Pineda, J. L., et al. 2011, *ApJ*, 741, 21, doi: [10.1088/0004-637X/741/1/21](https://doi.org/10.1088/0004-637X/741/1/21)
- Chuard, D., Terrier, R., Goldwurm, A., et al. 2018, *A&A*, 610, A34, doi: [10.1051/0004-6361/201731864](https://doi.org/10.1051/0004-6361/201731864)
- Churazov, E., Khabibullin, I., Sunyaev, R., & Ponti, G. 2017, *MNRAS*, 465, 45, doi: [10.1093/mnras/stw2750](https://doi.org/10.1093/mnras/stw2750)
- Churazov, E., Khabibullin, I., Barnouin, T., et al. 2024, *A&A*, 686, A14, doi: [10.1051/0004-6361/202349080](https://doi.org/10.1051/0004-6361/202349080)
- Clavel, M., Terrier, R., Goldwurm, A., et al. 2013, *A&A*, 558, A32, doi: [10.1051/0004-6361/201321667](https://doi.org/10.1051/0004-6361/201321667)
- Crocker, R. M. 2012, in *The Spectral Energy Distribution of Galaxies - SED 2011*, ed. R. J. Tuffs & C. C. Popescu, Vol. 284, 371–378, doi: [10.1017/S1743921312009441](https://doi.org/10.1017/S1743921312009441)
- Dahmen, G., Huttemeister, S., Wilson, T. L., & Mauersberger, R. 1998, *A&A*, 331, 959, doi: [10.48550/arXiv.astro-ph/9711117](https://doi.org/10.48550/arXiv.astro-ph/9711117)
- Dharmawardena, T. E., Bailer-Jones, C. A. L., Foesneau, M., et al. 2023, *MNRAS*, 519, 228, doi: [10.1093/mnras/stac2790](https://doi.org/10.1093/mnras/stac2790)
- Ferrière, K., Gillard, W., & Jean, P. 2007, *A&A*, 467, 611, doi: [10.1051/0004-6361:20066992](https://doi.org/10.1051/0004-6361:20066992)
- Foley, M. M., Goodman, A., Zucker, C., et al. 2023, *ApJ*, 947, 66, doi: [10.3847/1538-4357/acb5f4](https://doi.org/10.3847/1538-4357/acb5f4)

² <http://www.astropy.org>

³ <http://www.dendrograms.org/>

- García-Burillo, S., Usero, A., Alonso-Herrero, A., et al. 2012, *A&A*, 539, A8, doi: [10.1051/0004-6361/201117838](https://doi.org/10.1051/0004-6361/201117838)
- Ginsburg, A., Henkel, C., Ao, Y., et al. 2016, *A&A*, 586, A50, doi: [10.1051/0004-6361/201526100](https://doi.org/10.1051/0004-6361/201526100)
- GRAVITY Collaboration, Abuter, R., Amorim, A., et al. 2019, *A&A*, 625, L10, doi: [10.1051/0004-6361/201935656](https://doi.org/10.1051/0004-6361/201935656)
- Griffin, M. J., Abergel, A., Abreu, A., et al. 2010, *A&A*, 518, L3, doi: [10.1051/0004-6361/201014519](https://doi.org/10.1051/0004-6361/201014519)
- Guesten, R., & Henkel, C. 1983, *A&A*, 125, 136
- Hatchfield, H. P., Sormani, M. C., Tress, R. G., et al. 2021, *ApJ*, 922, 79, doi: [10.3847/1538-4357/ac1e89](https://doi.org/10.3847/1538-4357/ac1e89)
- Hatchfield, H. P., Battersby, C., Barnes, A. T., et al. 2024, *ApJ*, 962, 14, doi: [10.3847/1538-4357/ad10af](https://doi.org/10.3847/1538-4357/ad10af)
- Henshaw, J. D., Barnes, A. T., Battersby, C., et al. 2023, in *Astronomical Society of the Pacific Conference Series*, Vol. 534, *Protostars and Planets VII*, ed. S. Inutsuka, Y. Aikawa, T. Muto, K. Tomida, & M. Tamura, 83, doi: [10.48550/arXiv.2203.11223](https://doi.org/10.48550/arXiv.2203.11223)
- Hunter, J. D. 2007, *Computing in Science & Engineering*, 9, 90, doi: [10.1109/MCSE.2007.55](https://doi.org/10.1109/MCSE.2007.55)
- Immer, K., Menten, K. M., Schuller, F., & Lis, D. C. 2012, *A&A*, 548, A120, doi: [10.1051/0004-6361/201219182](https://doi.org/10.1051/0004-6361/201219182)
- Joye, W. A., & Mandel, E. 2003, in *Astronomical Society of the Pacific Conference Series*, Vol. 295, *Astronomical Data Analysis Software and Systems XII*, ed. H. E. Payne, R. I. Jedrzejewski, & R. N. Hook, 489
- Khabibullin, I., Churazov, E., & Sunyaev, R. 2022, *MNRAS*, 509, 6068, doi: [10.1093/mnras/stab3333](https://doi.org/10.1093/mnras/stab3333)
- Koyama, K. 2018, *PASJ*, 70, R1, doi: [10.1093/pasj/psx084](https://doi.org/10.1093/pasj/psx084)
- Koyama, K., Maeda, Y., Sonobe, T., et al. 1996, *PASJ*, 48, 249, doi: [10.1093/pasj/48.2.249](https://doi.org/10.1093/pasj/48.2.249)
- Krieger, N., Ott, J., Beuther, H., et al. 2017, *ApJ*, 850, 77, doi: [10.3847/1538-4357/aa951c](https://doi.org/10.3847/1538-4357/aa951c)
- Kruijssen, J. M. D., Dale, J. E., & Longmore, S. N. 2015, *MNRAS*, 447, 1059, doi: [10.1093/mnras/stu2526](https://doi.org/10.1093/mnras/stu2526)
- Kruijssen, J. M. D., & Longmore, S. N. 2013a, *MNRAS*, 435, 2598, doi: [10.1093/mnras/stt1634](https://doi.org/10.1093/mnras/stt1634)
- . 2013b, *MNRAS*, 435, 2598, doi: [10.1093/mnras/stt1634](https://doi.org/10.1093/mnras/stt1634)
- Lipman, D., Battersby, C., Walker, D. L., et al. 2024, *arXiv e-prints*, arXiv:2410.17321, doi: [10.48550/arXiv.2410.17321](https://doi.org/10.48550/arXiv.2410.17321)
- Longmore, S. N., Bally, J., Testi, L., et al. 2013, *MNRAS*, 429, 987, doi: [10.1093/mnras/sts376](https://doi.org/10.1093/mnras/sts376)
- Marin, F., Churazov, E., Khabibullin, I., et al. 2023, *Nature*, 619, 41, doi: [10.1038/s41586-023-06064-x](https://doi.org/10.1038/s41586-023-06064-x)
- Martín-Pintado, J., de Vicente, P., Fuente, A., & Planesas, P. 1997, *ApJL*, 482, L45, doi: [10.1086/310691](https://doi.org/10.1086/310691)
- McClure-Griffiths, N. M., Dickey, J. M., Gaensler, B. M., et al. 2012, *ApJS*, 199, 12, doi: [10.1088/0067-0049/199/1/12](https://doi.org/10.1088/0067-0049/199/1/12)
- Mills, E. A. C., Ginsburg, A., Immer, K., et al. 2018, *ApJ*, 868, 7, doi: [10.3847/1538-4357/aae581](https://doi.org/10.3847/1538-4357/aae581)
- Molinari, S., Swinyard, B., Bally, J., et al. 2010, *A&A*, 518, L100, doi: [10.1051/0004-6361/201014659](https://doi.org/10.1051/0004-6361/201014659)
- Molinari, S., Bally, J., Noriega-Crespo, A., et al. 2011, *ApJL*, 735, L33, doi: [10.1088/2041-8205/735/2/L33](https://doi.org/10.1088/2041-8205/735/2/L33)
- Molinari, S., Schisano, E., Elia, D., et al. 2016, *A&A*, 591, A149, doi: [10.1051/0004-6361/201526380](https://doi.org/10.1051/0004-6361/201526380)
- Muno, M. P., Baganoff, F. K., Bautz, M. W., et al. 2003, *ApJ*, 589, 225, doi: [10.1086/374639](https://doi.org/10.1086/374639)
- Muno, M. P., Bauer, F. E., Baganoff, F. K., et al. 2009, *ApJS*, 181, 110, doi: [10.1088/0067-0049/181/1/110](https://doi.org/10.1088/0067-0049/181/1/110)
- Murakami, H., Koyama, K., Sakano, M., Tsujimoto, M., & Maeda, Y. 2000, *ApJ*, 534, 283, doi: [10.1086/308717](https://doi.org/10.1086/308717)
- Nishiyama, S., Nagata, T., Tamura, M., et al. 2008, *ApJ*, 680, 1174, doi: [10.1086/587791](https://doi.org/10.1086/587791)
- Novak, G., Chuss, D. T., Renbarger, T., et al. 2003, *ApJL*, 583, L83, doi: [10.1086/368156](https://doi.org/10.1086/368156)
- Oka, T., Hasegawa, T., Handa, T., Hayashi, M., & Sakamoto, S. 1996, *ApJ*, 460, 334, doi: [10.1086/176973](https://doi.org/10.1086/176973)
- Oka, T., Hasegawa, T., Sato, F., Tsuboi, M., & Miyazaki, A. 1998, *ApJS*, 118, 455, doi: [10.1086/313138](https://doi.org/10.1086/313138)
- Park, S., Muno, M. P., Baganoff, F. K., et al. 2004, *ApJ*, 603, 548, doi: [10.1086/381542](https://doi.org/10.1086/381542)
- Pillai, T., Kauffmann, J., Tan, J. C., et al. 2015, *ApJ*, 799, 74, doi: [10.1088/0004-637X/799/1/74](https://doi.org/10.1088/0004-637X/799/1/74)
- Poglitsch, A., Waelkens, C., Geis, N., et al. 2010, *A&A*, 518, L2, doi: [10.1051/0004-6361/201014535](https://doi.org/10.1051/0004-6361/201014535)
- Ponti, G., Terrier, R., Goldwurm, A., Belanger, G., & Trap, G. 2010, *ApJ*, 714, 732, doi: [10.1088/0004-637X/714/1/732](https://doi.org/10.1088/0004-637X/714/1/732)
- Ponti, G., Morris, M. R., Terrier, R., et al. 2015, *MNRAS*, 453, 172, doi: [10.1093/mnras/stv1331](https://doi.org/10.1093/mnras/stv1331)
- Predehl, P., Sunyaev, R. A., Becker, W., et al. 2020, *Nature*, 588, 227, doi: [10.1038/s41586-020-2979-0](https://doi.org/10.1038/s41586-020-2979-0)
- Purcell, C. R., Longmore, S. N., Walsh, A. J., et al. 2012, *MNRAS*, 426, 1972, doi: [10.1111/j.1365-2966.2012.21800.x](https://doi.org/10.1111/j.1365-2966.2012.21800.x)
- Roman-Duval, J., Heyer, M., Brunt, C. M., et al. 2016, *ApJ*, 818, 144, doi: [10.3847/0004-637X/818/2/144](https://doi.org/10.3847/0004-637X/818/2/144)
- Schödel, R., Najarro, F., Muzic, K., & Eckart, A. 2010, *A&A*, 511, A18, doi: [10.1051/0004-6361/200913183](https://doi.org/10.1051/0004-6361/200913183)
- Seymour, N., Dwelly, T., Moss, D., et al. 2008, *MNRAS*, 386, 1695, doi: [10.1111/j.1365-2966.2008.13166.x](https://doi.org/10.1111/j.1365-2966.2008.13166.x)
- Sofue, Y. 1995, *PASJ*, 47, 527, <https://arxiv.org/abs/astro-ph/9508110>
- . 2000, *ApJ*, 540, 224, doi: [10.1086/309297](https://doi.org/10.1086/309297)
- Sofue, Y., & Handa, T. 1984, *Nature*, 310, 568, doi: [10.1038/310568a0](https://doi.org/10.1038/310568a0)

- Sormani, M. C., & Barnes, A. T. 2019, *MNRAS*, 484, 1213, doi: [10.1093/mnras/stz046](https://doi.org/10.1093/mnras/stz046)
- Sormani, M. C., Binney, J., & Magorrian, J. 2015, *MNRAS*, 449, 2421, doi: [10.1093/mnras/stv441](https://doi.org/10.1093/mnras/stv441)
- Sormani, M. C., Treß, R. G., Glover, S. C. O., et al. 2019, *MNRAS*, 488, 4663, doi: [10.1093/mnras/stz2054](https://doi.org/10.1093/mnras/stz2054)
- Su, Y., Zhang, S., Sun, Y., et al. 2024, *ApJL*, 971, L6, doi: [10.3847/2041-8213/ad656d](https://doi.org/10.3847/2041-8213/ad656d)
- Sunyaev, R., & Churazov, E. 1998, *MNRAS*, 297, 1279, doi: [10.1046/j.1365-8711.1998.01684.x](https://doi.org/10.1046/j.1365-8711.1998.01684.x)
- Sunyaev, R. A., Markevitch, M., & Pavlinsky, M. 1993, *ApJ*, 407, 606, doi: [10.1086/172542](https://doi.org/10.1086/172542)
- Terrier, R., Clavel, M., Soldi, S., et al. 2018, *A&A*, 612, A102, doi: [10.1051/0004-6361/201730837](https://doi.org/10.1051/0004-6361/201730837)
- Terrier, R., Ponti, G., Bélanger, G., et al. 2010, *ApJ*, 719, 143, doi: [10.1088/0004-637X/719/1/143](https://doi.org/10.1088/0004-637X/719/1/143)
- Walker, D. L., Battersby, C., Lipman, D., et al. 2024, arXiv e-prints, arXiv:2410.17320, doi: [10.48550/arXiv.2410.17320](https://doi.org/10.48550/arXiv.2410.17320)
- Walsh, A. J., Breen, S. L., Britton, T., et al. 2011, *MNRAS*, 416, 1764, doi: [10.1111/j.1365-2966.2011.19115.x](https://doi.org/10.1111/j.1365-2966.2011.19115.x)
- Wang, Q. D., Gotthelf, E. V., & Lang, C. C. 2002, *Nature*, 415, 148, doi: [10.1038/415148a](https://doi.org/10.1038/415148a)
- Zhang, S., Zhu, Z., Li, H., et al. 2020, *ApJ*, 893, 3, doi: [10.3847/1538-4357/ab7dc1](https://doi.org/10.3847/1538-4357/ab7dc1)
- Zhu, Z., Li, Z., & Morris, M. R. 2018, *ApJS*, 235, 26, doi: [10.3847/1538-4365/aab14f](https://doi.org/10.3847/1538-4365/aab14f)
- Zucker, C., Goodman, A., Alves, J., et al. 2021, *ApJ*, 919, 35, doi: [10.3847/1538-4357/ac1f96](https://doi.org/10.3847/1538-4357/ac1f96)